AGU PUBLICATIONS

JGR

Journal of Geophysical Research: Space Physics

RESEARCH ARTICLE
10.1002/2017JA024741

Key Points:
- To separate different escape channel, we have modified the MSE coordinate system
- Fluxes of the low-energy and high-energy oxygen ions reveal different trends with changes in solar wind
- The main driver for escape of the high-energy oxygen ions is the solar wind flux (or dynamic pressure)

Correspondence to:
E. Dubinin,
dubinin@mps.mpg.de

Citation:
Dubinin, E., Fraenz, M., Pätzold, M., McFadden, J., Halekas, J. S., DiBraccio, G. A., … Zelenyi, L. (2017). The effect of solar wind variations on the escape of oxygen ions from Mars through different channels: MAVEN observations. *Journal of Geophysical Research: Space Physics*, *122*. https://doi.org/10.1002/2017JA024741

Received 4 SEP 2017
Accepted 23 OCT 2017
Accepted article online 30 OCT 2017

The Effect of Solar Wind Variations on the Escape of Oxygen Ions From Mars Through Different Channels: MAVEN Observations

E. Dubinin[1], M. Fraenz[1], M. Pätzold[2], J. McFadden[3], J. S. Halekas[4], G. A. DiBraccio[5], J. E. P. Connerney[5], F. Eparvier[6], D. Brain[6], B. M. Jakosky[6], O. Vaisberg[7], and L. Zelenyi[7]

[1]Max Planck Institute for Solar System Research, Göttingen, Germany, [2]Rheinisches Institut fuer Umweltforschung, Abteilung Planetforschung, Cologne, Germany, [3]Space Sciences Laboratory, University of California, Berkeley, CA, USA, [4]Department of Physics and Astronomy, University of Iowa, Iowa City, IA, USA, [5]NASA Goddard Space Flight Center, Greenbelt, MD, USA, [6]Laboratory for Atmospheric and Space Physics, University of Colorado Boulder, Boulder, CO, USA, [7]Institute of Space Research, Moscow, Russia

Abstract We present multi-instrument observations of the effects of solar wind on ion escape fluxes on Mars based on the Mars Atmosphere and Volatile EvolutioN (MAVEN) data from 1 November 2014 to 15 May 2016. Losses of oxygen ions through different channels (plasma sheet, magnetic lobes, boundary layer, and ion plume) as a function of the solar wind and the interplanetary magnetic field variations were studied. We have utilized the modified Mars Solar Electric (MSE) coordinate system for separation of the different escape routes. Fluxes of the low-energy (≤30 eV) and high-energy (≥30 eV) ions reveal different trends with changes in the solar wind dynamic pressure, the solar wind flux, and the motional electric field. Major oxygen fluxes occur through the tail of the induced magnetosphere. The solar wind motional electric field produces an asymmetry in the ion fluxes and leads to different relations between ion fluxes supplying the tail from the different hemispheres and the solar wind dynamic pressure (or flux) and the motional electric field. The main driver for escape of the high-energy oxygen ions is the solar wind flux (or dynamic pressure). On the other hand, the low-energy ion component shows the opposite trend: ion flux decreases with increasing solar wind flux. As a result, the averaged total oxygen ion fluxes reveal a low variability with the solar wind strength. The large standard deviations from the averages values of the escape fluxes indicate the existence of mechanisms which can enhance or suppress the efficiency of the ion escape. It is shown that the Martian magnetosphere possesses the properties of a combined magnetosphere which contains different classes of field lines. The existence of the closed magnetic field lines in the near-Mars tail might be responsible for suppression of the ion escape fluxes.

Plain Language Summary In the past Mars was wet and the problem of its present dehydration is open. It is thought that the solar wind could blow off the volatiles at Mars. In the past solar wind was much stronger and we should know how escape of planetary ions forced by solar wind depends on the solar wind parameters. Using the data from the Mars Atmosphere and Volatile EvolutioN spacecraft, we study relations between ion fluxes of oxygen ions and solar wind and the interplanetary magnetic field characteristics.

1. Introduction

The interaction of solar wind with Mars starts at large distances from the planet where the newly ionized hydrogen and oxygen atoms originating in the extended hydrogen atmosphere and hot oxygen corona are picked up by the solar wind (Barabash et al., 1991; Dubinin, Fraenz, et al., 2006; Rahmati et al., 2015, 2017; Yamauchi et al., 2006, 2015). These ions are accelerated by the motional electric field $E = -v \times B$ and move on cycloidal trajectories. O^+ ions picked up in the magnetosheath and accelerated along the solar wind electric field form a plume in the Martian hemisphere defined by the positive direction of the solar wind electric field. Ions escaping through this channel contribute about 20% of the total ion losses (Dong et al., 2015). Closer to Mars, the solar wind interacts directly with the ionosphere forming the draped induced magnetosphere. The draped interplanetary magnetic field (IMF) field lines in the wake shape the long tail on the night side (Nagy et al., 2004; Dubinin & Fraenz, 2015). The well-organized structure of the induced magnetic tail contains

two important channels for ion escape. Stretched field lines in the lobes with the central parts inside the magnetized Martian ionosphere are a pathway for ions extracted by the parallel ambipolar electric field (Dubinin et al., 2011; Collinson et al., 2015). The tail lobes with oppositely directed magnetic field lines are separated by a plasma sheet in which the planetary ions gain additional acceleration by the $j \times B$ force (Barabash et al., 2007; Dubinin & Fraenz, 2015; Dubinin et al., 1993, 2013; Fedorov et al., 2006, 2008; Halekas et al., 2006). The existence of strong localized crustal magnetic fields (Acuña et al., 1998) influences the interaction of the solar wind with the ionosphere causing in addition to the draping IMF, new classes of field lines—closed field lines and open lines with one end in the solar wind and another one in the collisional atmosphere (Brain et al., 2003; Fang et al., 2015; Luhmann et al., 2017; Ma et al., 2014; Xu et al., 2016; 2017). This very complicated magnetic field geometry not only affects the existing escape routes but also produces new channels for escape of planetary ions. For example, by analyzing the pitch angle distribution of photoelectrons, Xu et al. (2017) have shown that the low-altitude ionosphere, even in the northern hemisphere, is largely permeated by closed field lines which prevent the ion transport to the tail. On the other hand, open field lines which are stretched in the tailward direction are similar to open field lines in the Earth magnetosphere and might be a potential route for polar wind at Mars (Collinson et al., 2015). Such a big variety of routes for ion escape makes it necessary to study the efficiency of ion losses depending on solar wind parameters by considering the role of the different escape channels. This goal also requires a proper choice of a coordinate system, which is adequate for the statistical description of the global picture of ion fluxes.

Solar wind and solar irradiance are the main drivers which control the atmospheric losses at Mars that might be important for the evolution of its atmosphere and water inventory. In this paper we study the dependence of ion fluxes on solar wind variations. Previous studies of this problem used the Analyzer of Space Plasmas and Energetic Atoms-3 (ASPERA-3) measurements on Mars Express (MEX) (Lundin et al., 2008; Nilsson et al., 2010, 2012; Ramstad et al., 2015). Based on the analysis of 42 selected orbits, Lundin et al. (2008) have observed a positive correlation between the solar wind dynamic pressure and ion fluxes in the Mars tail ($F_i \sim P_{\mathrm{dyn}}^{0.41}$). Assuming rotational symmetry of the escape area, Lundin et al. (2008) estimated the long-term variations in the total losses due to changes in solar wind dynamic pressure by a factor of 25–30. Nilsson et al. (2010) analyzed the data obtained by MEX in 2006 when the ASPERA-3 instrument did not yet measure the low-energy ($E_i < 30–50$ eV) ion component and found a positive correlation of ion fluxes with the value of the subsolar magnetic field inferred from Mars Global Surveyor (MGS) observations on the dayside at an altitude of 400 km and extrapolated to the subsolar point. The total ion losses increased by a factor of 2–3 for high values (>41 nT) of the subsolar magnetic field. Nilsson et al. (2010) have also observed that the average ion flux was 2–3 times higher in the E^+ hemisphere as defined by the direction of the solar wind motional electric field. Nilsson et al. (2011) analyzed the ASPERA-3 data obtained between May 2007 and May 2011 using a new approach based on the calculation of the ion distribution function averaged in each spatial bin. By comparing the escape ion fluxes in the tail for low and high solar wind fluxes, Nilsson et al. (2011) have observed an enhancement of the ion fluxes in the central part of the tail but a reduction in the outer magnetospheric regions during the periods of high solar wind fluxes. Correspondingly, the net increase was only ~20%. Dubinin et al. (2011) and Dubinin and Fraenz (2015) discussed a correlation between the solar wind dynamic pressure and ion fluxes in the plasma sheet for a 2 week interval of MEX observations. Ion fluxes varied by a factor of ~10 in response to solar wind variations. The results have confirmed the hypothesis of a chain of processes whereby the solar wind momentum is transferred to the magnetic field pressure on the dayside and then via the magnetic field stresses on the nightside to the momentum of planetary ions. Ramstad et al. (2015) investigated variations of ion losses as a function of the solar wind density at fixed values of the solar wind velocity and solar irradiance. The authors have found a trend of an increase in the total escape rate with decreasing solar wind density. Such contradictory results make it necessary to further examine this problem which is closely related to the global problem of the Mars dehydration. In past epochs solar wind was stronger and solar irradiance was higher and therefore we need to know how escape fluxes depend on variations of solar wind and solar EUV. Effects of solar irradiance on escape ion fluxes were recently discussed in Ramstad et al. (2015), Dubinin, Fraenz, Pätzold, Andrews, et al. (2017), and Dubinin, Fraenz, Pätzold, McFadden, et al. (2017). Here we will focus on effects related to variations in the solar wind that are important for ion escape forced by the solar wind. The measurements made by the Mars Atmosphere and Volatile EvolutioN (MAVEN) spacecraft provide the opportunity to study these processes with simultaneous monitoring of solar wind and the IMF in more detail.

2. Observations

2.1. Instrumentation

The MAVEN spacecraft arrived at Mars in September 2014 to study the processes in the upper atmosphere/ionosphere and its interaction with solar wind (Jakosky et al., 2015). MAVEN was inserted into an elliptical orbit with periapsis and apoapsis of 150 km and 6,200 km, respectively, and with a period of 4.5 h. The spacecraft carries nine sensors which measure the input fluxes of solar wind and solar irradiance and monitor the response of the Martian atmosphere/exosphere and ionosphere on these driving inputs. In this paper we use data from four instruments to study effects of the variability in the solar wind on the structure of the Martian magnetosphere and ion losses for the period 1 November 2014 to 15 May 2016.

The Supra-Thermal And Thermal Ion Composition (STATIC) instrument mounted on the Actuated Payload Platform (APP) is used to study the escape of planetary ions. It measures energy spectra of ion fluxes in the range of 0.1 eV–30 keV and the ion composition (McFadden et al., 2015). The instrument consists of a toroidal top hat electrostatic spectrometer with an electrostatic deflector at the entrance providing 360° × 90° field of view combined with a time-of-flight velocity analyzer resolving the major ion species H^+, He^{++}, He^+, O^+, O_2^+, and CO_2^+. The measurements allow a retrieval of the velocity distribution functions and their moments (density, velocity, and temperature) for different ion species. The measurements of the low-energy ions in the dense ionosphere and in the planetary wake are affected by the negative spacecraft potential. Therefore, calculating the ion distribution functions, we made corrections using the spacecraft potential. Corrections related to the spacecraft velocity were also applied. The instrument operates in different modes (RAM, Conic, and Pickup) providing different data products with different mass, energy, angular, and time resolution. In this study we used "joined" products which have 32 energy steps, 4 deflector angles (elevation angles), 16 anodes (azimuth angles), 8 ion masses, and 4 s cadence to calculate the moments of the ion distribution functions.

The measurements made by the Solar Wind Ion Analyzer (SWIA) (Halekas et al., 2015) and the MAG (magnetometer) (Connerney et al., 2015) were used to monitor the solar wind and the interplanetary magnetic field (IMF). SWIA provides the solar wind parameters with a cadence of 4 s. We also used the magnetic field data from two independent triaxial fluxgate magnetometers (MAG) mounted on the booms of the MAVEN spacecraft (Connerney et al., 2015).

We have also utilized the data (L3 data product) from the Extreme Ultraviolet Monitor on the MAVEN (Eparvier et al., 2015) to determine the solar irradiance.

We utilize the MAG data in the MSO and MSE coordinates. The Mars Solar Orbital (MSO) coordinates have the X_{MSO} axis directed from the center of Mars to Sun. The Y_{MSO} axis is opposite to the direction of the orbital Mars velocity, and the Z_{MSO} axis completes the right-handed system. In the Mars Solar Electric system the X_{MSE} axis coincides with the X_{MSO} axis, while the Y_{MSE} axis is determined by the magnetic field vector in the solar wind being along the cross-flow component of the IMF. Then the Z_{MSE} axis is always along the direction of the motional electric field $E_{sw} = -V_{sw} \times B_{IMF}$. We took the IMF orientation on each MAVEN orbit by averaging the MAG data in the upstream solar wind over 30 min. In contrast to the approach by Halekas et al. (2017) we did not use very strict criteria on the MAG data ensuring only the periods with steady and undisturbed IMF orientation. We processed all orbits in order to study the global features of the Martian magnetosphere without any simplifying assumptions.

2.2. Selection of the Coordinate Frame

To study the relationship between ion fluxes through different escape channels and solar wind conditions, we need, at first, to choose the coordinate system which is more appropriate to describe the global picture of ion fluxes. For example, a cylindrical coordinate system is often used to characterize the flow pattern at Mars (see, e.g., Fraenz et al., 2015; Lundin et al., 2008; Nilsson et al., 2010, 2011; Ramstad et al., 2015). Figures 1a and 1b show maps of the mean values of fluxes of O^+ ions with $E > 30$ eV and $E < 30$ eV, respectively, in cylindrical coordinates. Fluxes occupy mainly the interior magnetosphere. It is also seen that fluxes of ions with lower energies dominate. A sharp drop of fluxes at the border of the wake appears due to a negative spacecraft potential in the shadow region which improves the chance to detect cold ionospheric ions. In contrast, a positive potential in the sunlit areas reduces the sensitivity of the instrument. Although a cylindrical coordinate system can adequately describe the values of total losses (see, e.g., Nordstrom et al., 2013) some important features are lost. In the MSE coordinates the distribution of the magnetic field around Mars becomes well organized (Dubinin & Fraenz, 2015; Yeroshenko et al., 1990). Moreover, an asymmetry of ion fluxes caused by the motional electric field can be displayed if we use the MSE coordinate system. Figures 1c and 1d show

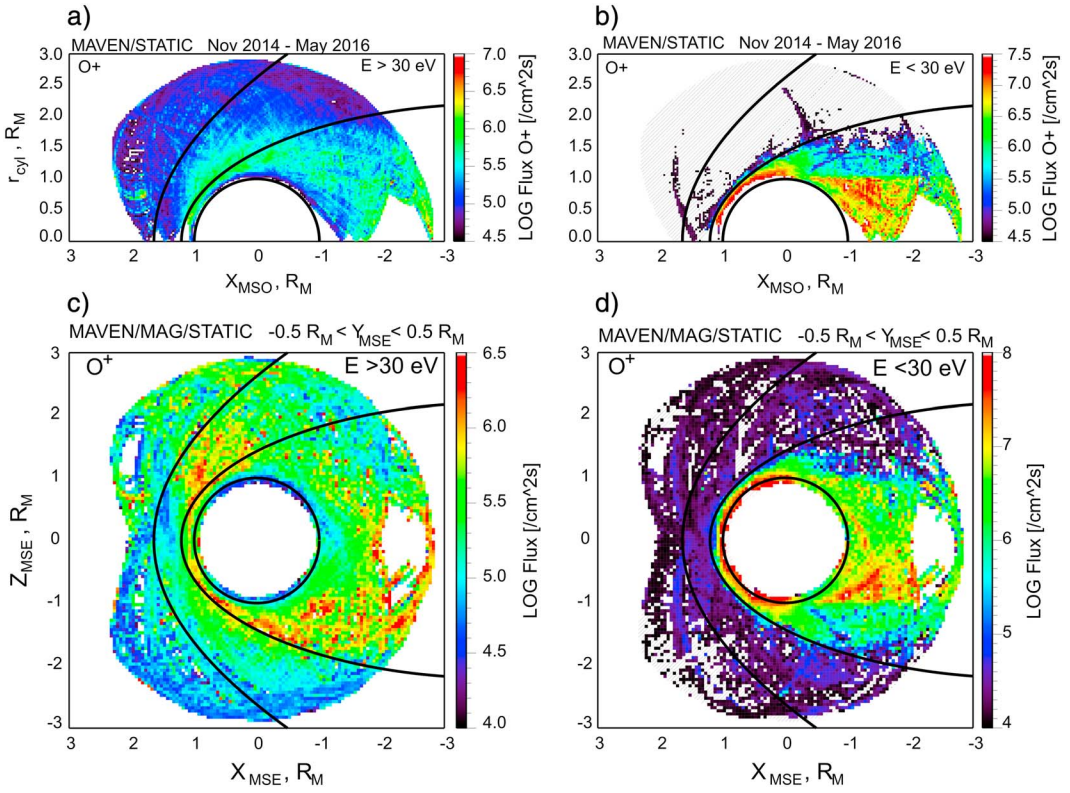

Figure 1. (a and b) Maps of the mean values of fluxes of O^+ ions with $E > 30$ eV and $E < 30$ eV, respectively, plotted in cylindrical coordinates. (c and d) Maps of the mean fluxes of O^+ ions with $E > 30$ eV and $E < 30$ eV, respectively, in the XZ_{MSE} plane. Nominal positions of the bow shock and the induced magnetosphere boundary (Dubinin, Franz, et al., 2006) are shown.

maps of the mean fluxes of O^+ ions with $E > 30$ eV and $E < 30$ eV, respectively, in the XZ_{MSE} plane. Note that the separation of ions into high- and low-energy components is based on previous analysis of the ion distribution functions in the Martian tail made by Nilsson et al. (2012) and Fräenz et al. (2015). It was shown that the typical ion distribution consists of two ion populations, low-energy ions whose energy almost does not vary in the tail and a more energetic component which accelerates downstream. Measurements made at $-0.5R_M < Y_{MSE} < 0.5R_M$ were used for the maps in Figures 1c and 1d. It is seen that ions extracted from the hot oxygen corona in the sheath and probably from the external ionosphere and moving on cycloidal trajectories produce an ion plume in the E^+ hemisphere ($Z_{MSE} > 0$) (Dong et al., 2015; Dubinin et al., 2011). Another escape channel visible in Figure 1c is caused by the inflow of O^+ ions to the wake in the E^- hemisphere ($Z_{MSE} < 0$). A map of the fluxes of the low-energy ions (Figure 1d) also reveals new interesting features. A shift of these fluxes toward the E^- hemisphere is clearly observed (see also Dubinin, Fraenz, Pätzold, McFadden, et al., 2017). Another important feature seen in Figure 1d is the filling of the nightside ionosphere by ion fluxes from the dayside.

To separate more clearly different regions in the tail, we can use another set of variables. Figure 2 shows maps of the proton and oxygen ion fluxes in the B_x-Z_{MSE} coordinates, where B_x is the X component of the magnetic field locally measured by MAG at $-2\,R_M < X < -1\,R_M$ and Z is the spacecraft coordinate in the MSE frame. A change of sign of the B_x component corresponds to the crossing of the central current sheet in the tail. This set of variables is useful since it allows to avoid the problem with multiple crossings of the current sheet due to its flapping motion (DiBraccio et al., 2017; Dubinin & Fraenz, 2015; Dubinin et al., 2012) and reduces uncertainties related to a time lag of the current sheet orientation in response to the IMF variations (Modolo et al., 2012). In Figure 2a we can clearly identify the magnetosheath and the plasma sheet with adjacent tail lobes. On the maps of oxygen fluxes we observe that the plasma sheet is filled by more energetic oxygen ions (Figure 2b), while the lobes mainly contain the lower energy component (Figure 2c). Such a separation occurs due to a focusing effect by ion acceleration by the $j \times B$ forces (Dubinin & Fraenz, 2015; Dubinin et al., 1993, 2011). It is also seen that fluxes of oxygen ions at the outer edges of the lobes (boundary layer) are mostly localized

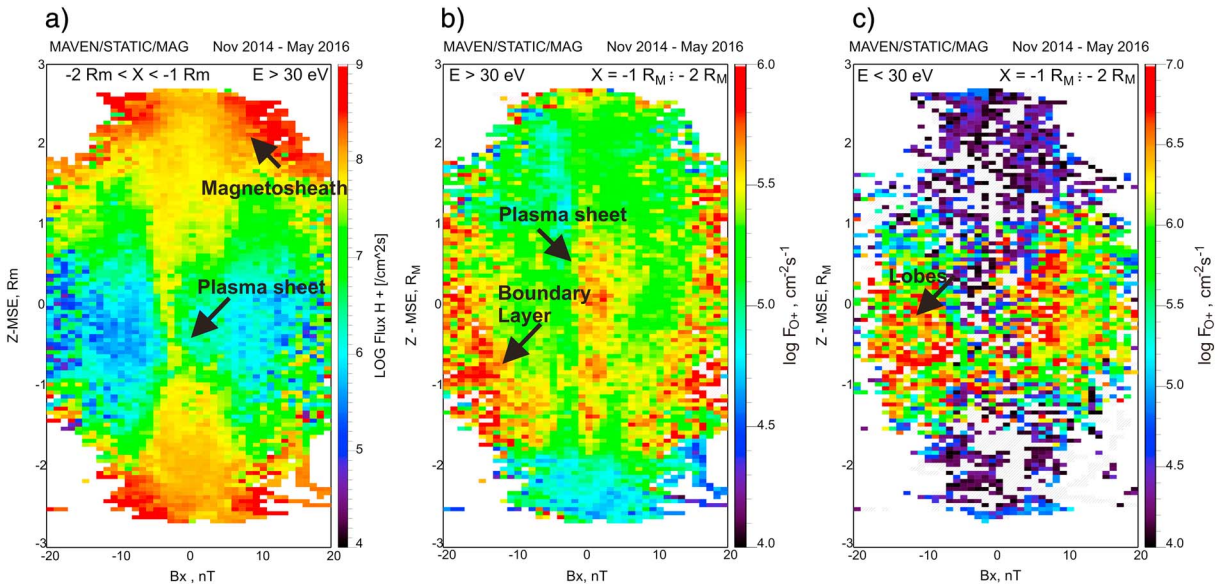

Figure 2. Maps of the proton and oxygen ion fluxes in the B_x-Z_{MSE} coordinates, where B_x is the X component of the magnetic field locally measured by MAG at $-2\,R_M < X < -1\,R_M$ and Z is the spacecraft coordinate in the MSE frame.

in the E^- hemisphere. It is worth noting that the fluxes of low-energy oxygen ions dominate over fluxes of the more energized component. In the following we will consider separately responses of fluxes of low- and high-energy oxygen ions on solar wind variations (see also Dubinin, Fraenz, Pätzold, Andrews, et al., 2017; Dubinin, Fraenz, Pätzold, McFadden, et al., 2017).

It is worth noting that the MSE (or the modified MSE) coordinate system is also not perfect for the description of the near-Mars space. When rotating the spacecraft trajectories onto MSE coordinates and making averaging the effects of the crustal magnetic field become less visible similar as it happens with the effects of the motional electric field in the cylindrical or in the MSO coordinates. The influence of the crustal fields on the dynamics of ion fluxes is rather complicated because of a very intricate topology of the field lines and the Mars rotation. Nevertheless, one may expect a global effect of the crustal fields on the magnetic topology near Mars while considering a statistical field configuration by averaging over many Mars rotations. Figure 3a shows a map of the mean value of the B_x component in the YZ_{MSO} plane at $-2\,R_M < X < 0\,R_M$ calculated from the Cain model (Cain et al., 2003) along the MAVEN orbits. Besides the localized area of the strong magnetic field in the southern hemisphere, we observe a weaker but global contribution with $B_x > 0$ ($B_x < 0$) in the northern (southern) hemisphere, respectively. This result appears due to low-order harmonics in the expansion of the model crustal magnetic field. The combination of the draping configuration of the induced magnetosphere and the field produced by the low-harmonics leads to a combined magnetosphere with elements of an induced and an intrinsic magnetospheres. The existence of this mixed magnetosphere was shown in model laboratory experiments (Dubinin et al., 1980). By tracing the halo solar wind electrons measured by the Phobos-2 spacecraft, Dubinin et al. (1994) have observed signatures which could be interpreted as the manifestation of the combined magnetosphere on Mars. The characteristic feature of the combined magnetosphere is the twist of the current sheet in the magnetic tail. The sign of this twist is determined by the orientation of the cross-flow component of the IMF. Figures 3b and 3c show maps of the B_x component of the magnetic field measured by MAG/MAVEN in the YZ_{MSO} plane ($-2\,R_M < X < 0\,R_M$) for cases with $B_y(\mathrm{IMF}) > 0$ and $B_y(\mathrm{IMF}) < 0$, respectively. The twist of the current sheet occurs in different directions in response to a change in sign of the B_y component in the solar wind that is in the agreement with features of the combined magnetosphere (Dubinin et al., 1980). Correspondingly, one may expect a twist of the plasma sheet. Maps of fluxes of O^+ ions with $E > 30$ eV are shown in Figures 3e and 3f. Plasma sheets filled by the accelerating O^+ ions follow the rotations of the current sheet though the distribution of ion fluxes at $B_y(\mathrm{IMF}) < 0$ occurs to be broadened. It is also worth to mention that the fluxes observed outside of the projection of the planet fill mainly the regions in the southern (northern) hemisphere for $B_y(\mathrm{IMF}) > 0$ ($B_y(\mathrm{IMF}) < 0$), respectively, following the direction of the $-E_{sw} = V_{sw} \times B_{IMF}$ vector. This result is confirmed by a map of ion fluxes in the YZ_{MSE} plane (Figure 3d). It is also seen (Figure 3d) that the plasma sheet in the MSE coordinates occurs rather

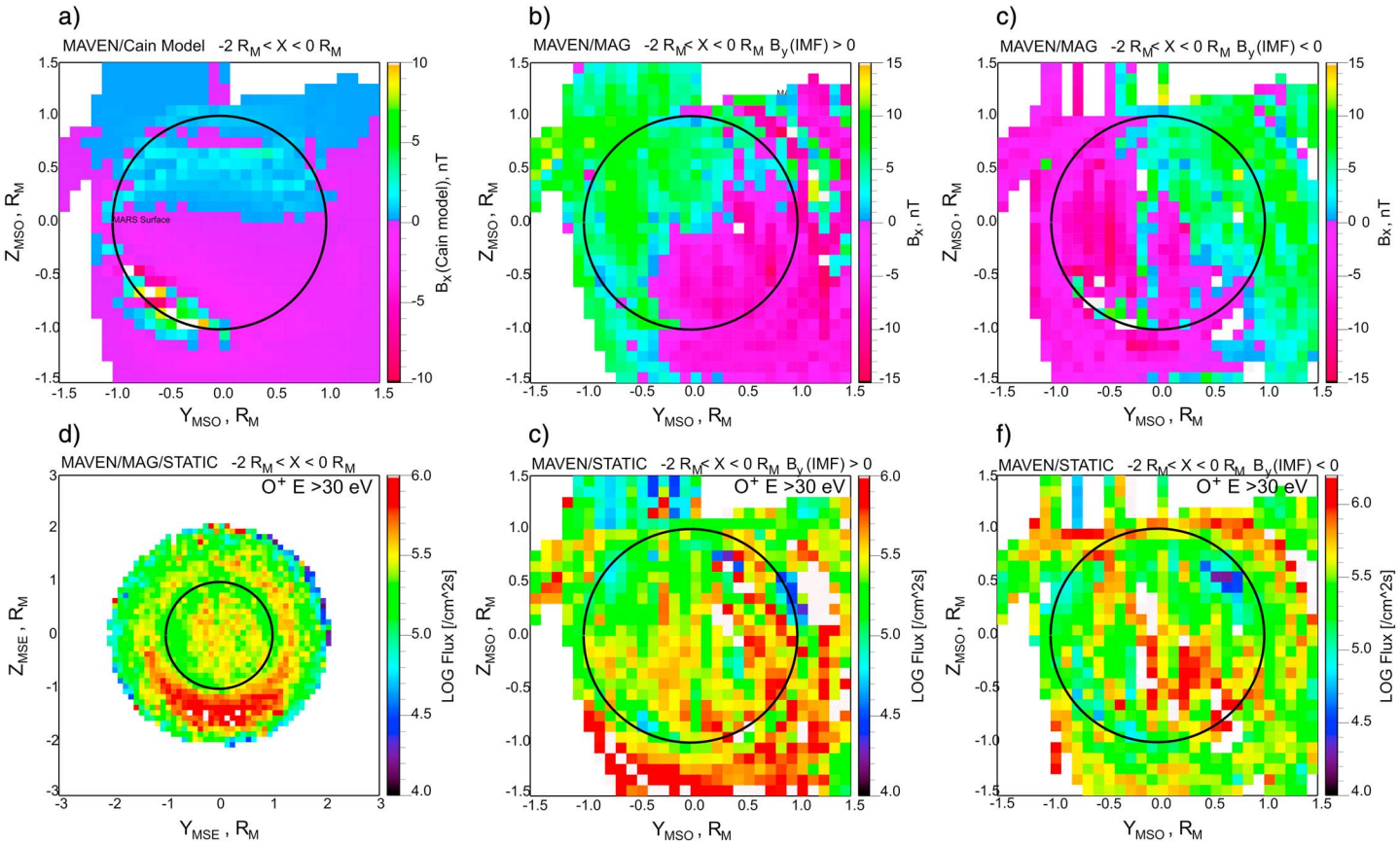

Figure 3. (a) Map of the mean value of the B_x component in the YZ_{MSO} plane at $-2\,R_M < X < 0\,R_M$ calculated from the Cain's model (Cain et al., 2003) along the MAVEN orbits; (b and c) maps of the B_x component of the magnetic field measured by MAG/MAVEN in the YZ_{MSO} plane ($-2\,R_M < X < 0\,R_M$) for cases with $B_y(\mathrm{IMF}) > 0$ ($B_y(\mathrm{IMF}) < 0$), respectively; (d) map of O^+ ion fluxes ($E > 30$ eV) in the YZ_{MSE} plane; (e and f) maps of fluxes of O^+ ions with $E > 30$ eV for cases with $B_y(\mathrm{IMF}) > 0$ ($B_y(\mathrm{IMF}) < 0$), respectively, plotted in the MSO frame.

diffused due to superposition of the maps in Figures 3e and 3f and the uncertainties with the MSE coordinates. Thus, using MSO coordinates and selecting MAVEN orbits with a fixed direction of B_y(IMF) reveals new features of the magnetic field and plasma environment near Mars. In this paper we use the modified MSE coordinate system and do not sort the different types of the field lines. This requires a more sophisticated analysis of the MAVEN data (see, e.g., Brain et al., 2007; Xu et al., 2017) to be done in a future study.

3. Variations of Ion Fluxes in Different Escape Channels as a Function of Solar Wind

3.1. Plasma Sheet

Figure 4 shows a map of fluxes of O^+ and O_2^+ ions with $E > 30$ eV observed within the Martian magnetosphere in the B_x-X coordinates, where X is the spacecraft coordinate in the MSO (MSE) reference frame. This "coordinate plane" might be considered as a modification of the XY_{MSE} plane. The plasma sheet is well displayed. Figure 4 (bottom row) depicts the plots of ion fluxes at $-1.6\,R_M < X < -1.2\,R_M$ across the tail as a function of B_x. Fluxes of both ion species are approximately equal, and therefore, in the following we will analyze only the fluxes of O^+ ions. To study the dependence of ion fluxes in the plasma sheet on solar wind parameters, we selected the interval of -10 nT $< B_x < 10$ nT in the tail (see Figure 4). Figure 5 shows how fluxes of O^+ ions vary with the variations in the solar wind dynamic pressure (Figure 5a), the solar wind ion flux (Figure 5b), the solar motional electric field ($-v \times B$) (Figure 5c). Figure 5 (bottom row) shows the data coverage in this parameter space. It is observed that at $X \gtrsim -2.5\,R_M$ fluxes of oxygen ions increase with an increase of the solar wind dynamic pressure and solar wind ion flux. We do not observe a visible correlation between the motional electric field and ion fluxes. Figure 6 shows mean values of fluxes of O^+ ions ($E > 30$ eV) and their standard deviations in the plasma sheet as a function of the solar wind and the IMF variations at the distances $-2\,R_M < X < -1\,R_M$ (black curves) and $-3\,R_M < X < -2.2\,R_M$ (blue curves), respectively. There are power law

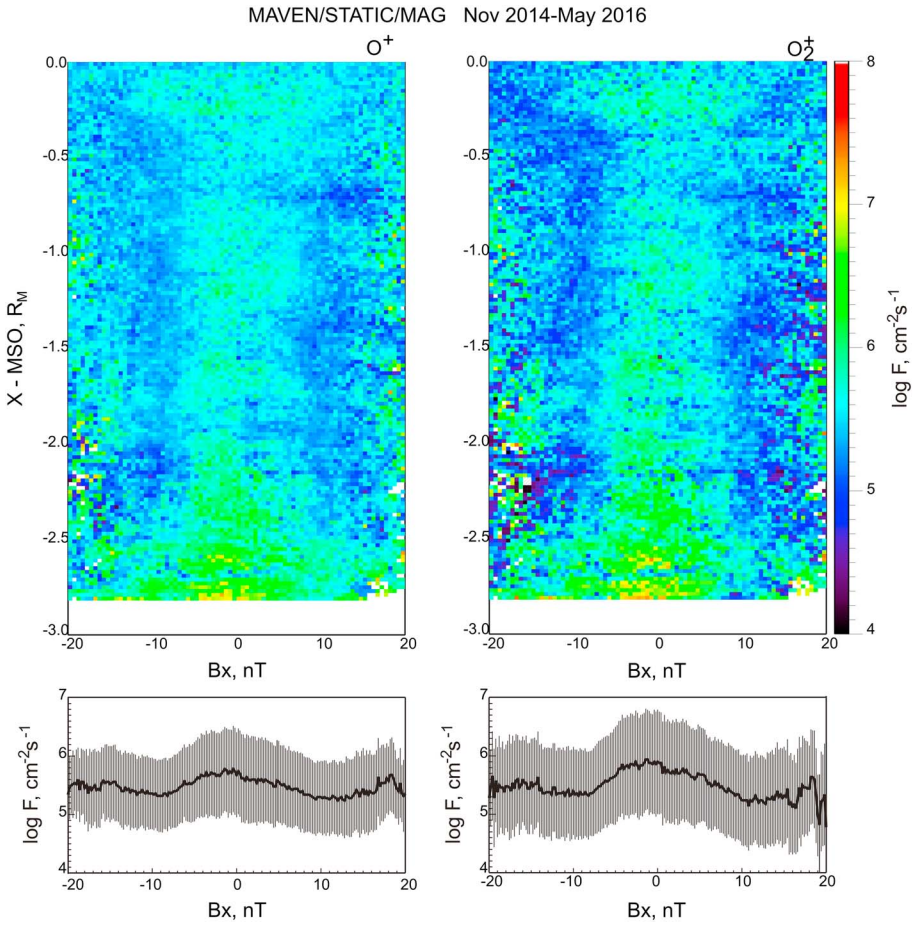

Figure 4. Map of fluxes of O^+ and O_2^+ ions with $E > 30$ eV observed in the Martian tail in the B_x-X coordinates, where X is the spacecraft coordinate in the MSO (MSE) reference frame. Plots on the bottom the plots of ion fluxes at $-1.6\,R_M < X < -1.2\,R_M$ across the tail as a function of B_x.

dependences $F_{O^+} \sim P_{dyn}^{0.73}$ and $F_{O^+} \sim F_{sw}^{0.86}$ at $-2\,R_M < X < -1\,R_M$. On the other hand, there is no almost correlation between the flux of O^+ ions ($E > 30$ eV) and variations of the motional electric field in the solar wind and the IMF orientation (the cone angle is the angle between the IMF vector and the X-MSO vector). With increase of $P_{dyn} = 0.05$ nPa to $P_{dyn} = 2$ nPa (or $F_{sw} = 2 \cdot 10^7$ cm^{-2} s^{-1} to $F_{sw} = 6.3 \cdot 10^8$ cm^{-2} s^{-1}) the mean values of O^+ ions ($E > 30$ eV) raise by a factor of 10. It is interesting to note that the dependence on the solar wind strength becomes stronger when we examine narrower layers of the plasma sheet (Figure 7). It is worth noting that with decrease of the examined plasma sheet with the effect of the dependence on the motional electric fields appears.

At larger distances ($-3\,R_M < X < -2.2\,R_M$) in the tail (see Figure 6) where we observe a general increase of ion fluxes (see, e.g., Figures 1 and 2) the dependences of F_{O^+} on P_{dyn} and F_{sw} are more complicated and are characterized not only by their growth with P_{dyn} and F_{sw} but also by an increase at low P_{dyn} and F_{sw}. Also, in contrast to closer distances to Mars, we observe a distinct correlation of F_{O^+} with the motional electric field. All these features indicate that the plasma sheet at large distances is supplied by another ion source with a different dependence on solar wind parameters. An inspection of Figure 1 locates this source in the E^- hemisphere.

3.2. Tail Lobes

It was shown that the tail lobes are mostly filled by low-energy ions (see, e.g., Figure 2c). Figure 8 compares the mean values of fluxes of O^+ ions with $E > 30$ eV (a–c) and $E < 30$ eV (d–f) across the tail as a function of the solar wind dynamic pressure (Figures 8a and 8d), the solar wind flux (Figures 8b and 8e), and the motional electric field in the solar wind (Figures 8c and 8f) at $-2\,R_M < X < -1\,R_M$. Different trends for ion fluxes of high- and low-energy ions are evident. With an increase in P_{dyn} and F_{sw}, fluxes of ions with higher-energy

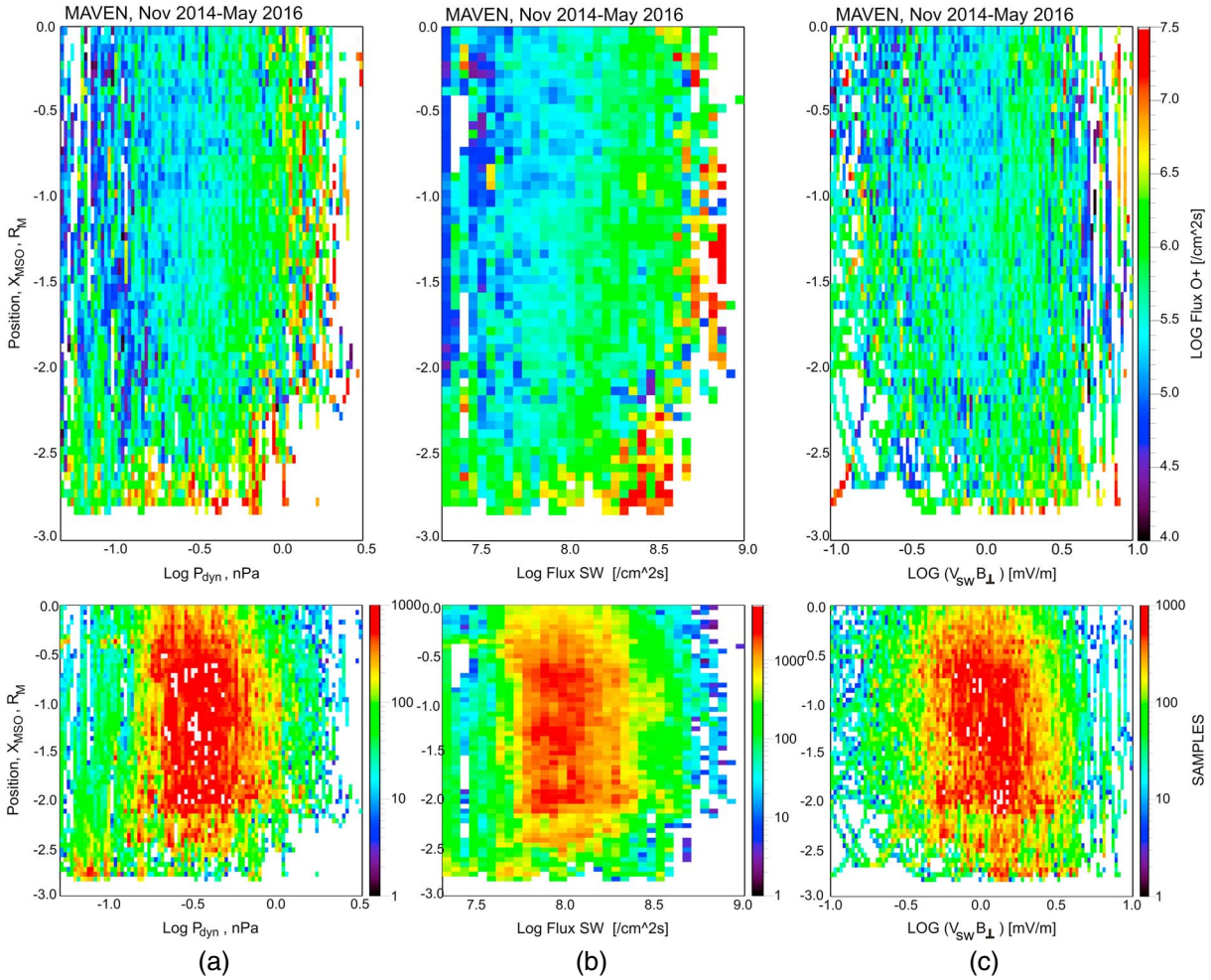

Figure 5. Maps of fluxes of O^+ ions ($E > 30$ eV) in the tail as a function of (a) the solar wind dynamic pressure, (b) the solar wind ion flux, and (c) the solar motional electric field ($-v \times B$). The bottom panels show the number of samples in each bin.

grow and the magnetic field in the tail increases. In contrast, fluxes of low-energy ions in the lobes decrease. Such a behavior can be explained by the enhanced energization of ions with an increase of the solar wind flux (dynamic pressure). It is also seen that at low levels of the solar wind flux (dynamic pressure), ions with $E < 30$ eV also occupy the plasma sheet. This happens because of the lower efficiency of ion energization in the plasma sheet. Then, at low values of P_{dyn} and F_{sw} when the magnetic field in the tail and, correspondingly, the magnetic tensions become smaller, ions in the plasma sheet are accelerated to lower energies. This means that the energy of separation between the low- and high-energy components must be smaller than 30 eV we have used above. Indeed, it occurs that if we take, for example, $E = 15$ eV, the low-energy ions ($E < 15$ eV) fill only the lobes. With the increase of P_{dyn} and F_{sw} the magnetic field in the tail increases (see Figure 8) and O^+ ions are accelerated to higher values. Figure 9 depicts the relationship between ion fluxes with $E < 30$ eV and P_{dyn}, F_{sw}, E_{sw}, and the cone angle. Except for very low values of the solar wind dynamic pressure and solar wind flux, there is a general trend of their decrease with increase of the solar wind strength. Dubinin, Fraenz, Pätzold, Andrews, et al. (2017) and Dubinin, Fraenz, Pätzold, McFadden, et al. (2017) have shown that the fluxes of the low-energy ions are sensitive to the solar EUV flux. To exclude a possible contribution of this driver, we have analyzed similar dependences for a fixed value (0.045 – 0.06 W/m^2) of the solar irradiance. The blue curve depicts the mean values of the ion fluxes. We observe the same trend of decrease of the ion fluxes with increase in the solar wind dynamic pressure, the solar wind ion flux, and the motional electric field.

3.3. Boundary Layer

The existence of a population of oxygen ions near the boundary of the induced magnetosphere (IMB) is displayed in Figures 1c and 2b. It is the region where solar wind is in direct contact with the ionosphere and where

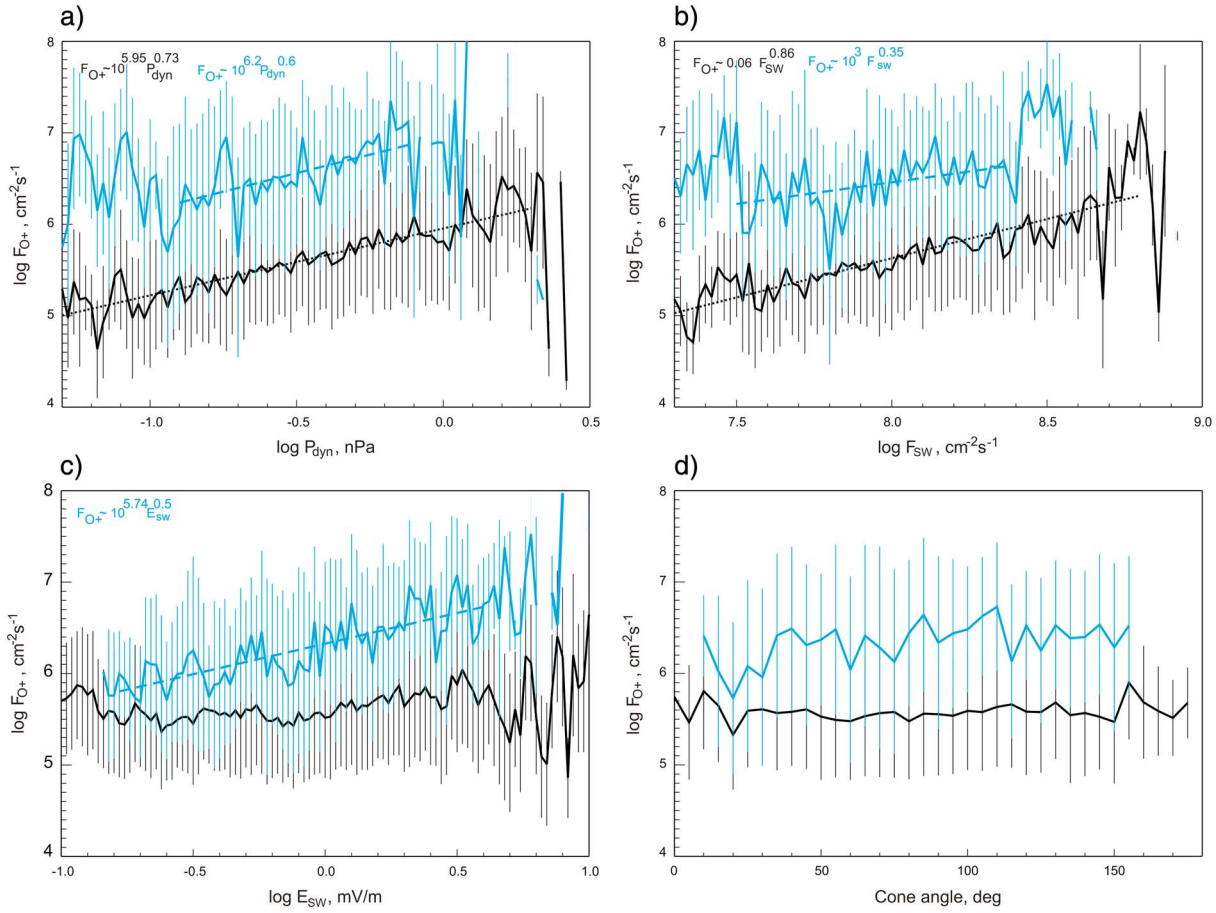

Figure 6. Mean values of fluxes of O^+ ions ($E > 30$ eV) and their standard deviations in the plasma sheet as a function of (a) the solar wind dynamic pressure, (b) the solar wind proton flux, (c) the motional electric field in the solar wind, and (d) the IMF variations (the cone angle) at distances $-2\,R_M < X < -1\,R_M$ (black curves) and $-3\,R_M < X < -2.2\,R_M$ (blue curves), respectively

the solar wind momentum is transferred to the ionospheric plasma. Although the existence of the boundary layer was shown long ago (Dubinin et al., 1996; Vaisberg, 1976), the mechanism of its formation is still open. Figure 1c shows that the ions in the boundary layer on the dayside are gradually transported inward the magnetosphere and fill the circular region behind the planet. The distribution of ions in this circular area

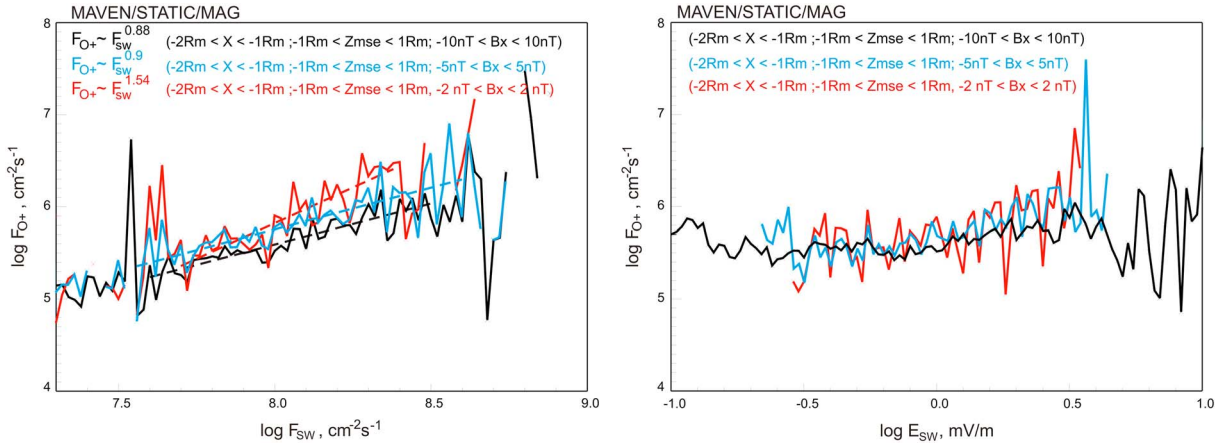

Figure 7. Mean values of fluxes of O^+ ions ($E > 30$ eV) in the plasma sheet as a function of the solar wind dynamic pressure and the motional electric field measured for different widths of the plasma sheet expressed by the considered B_x interval.

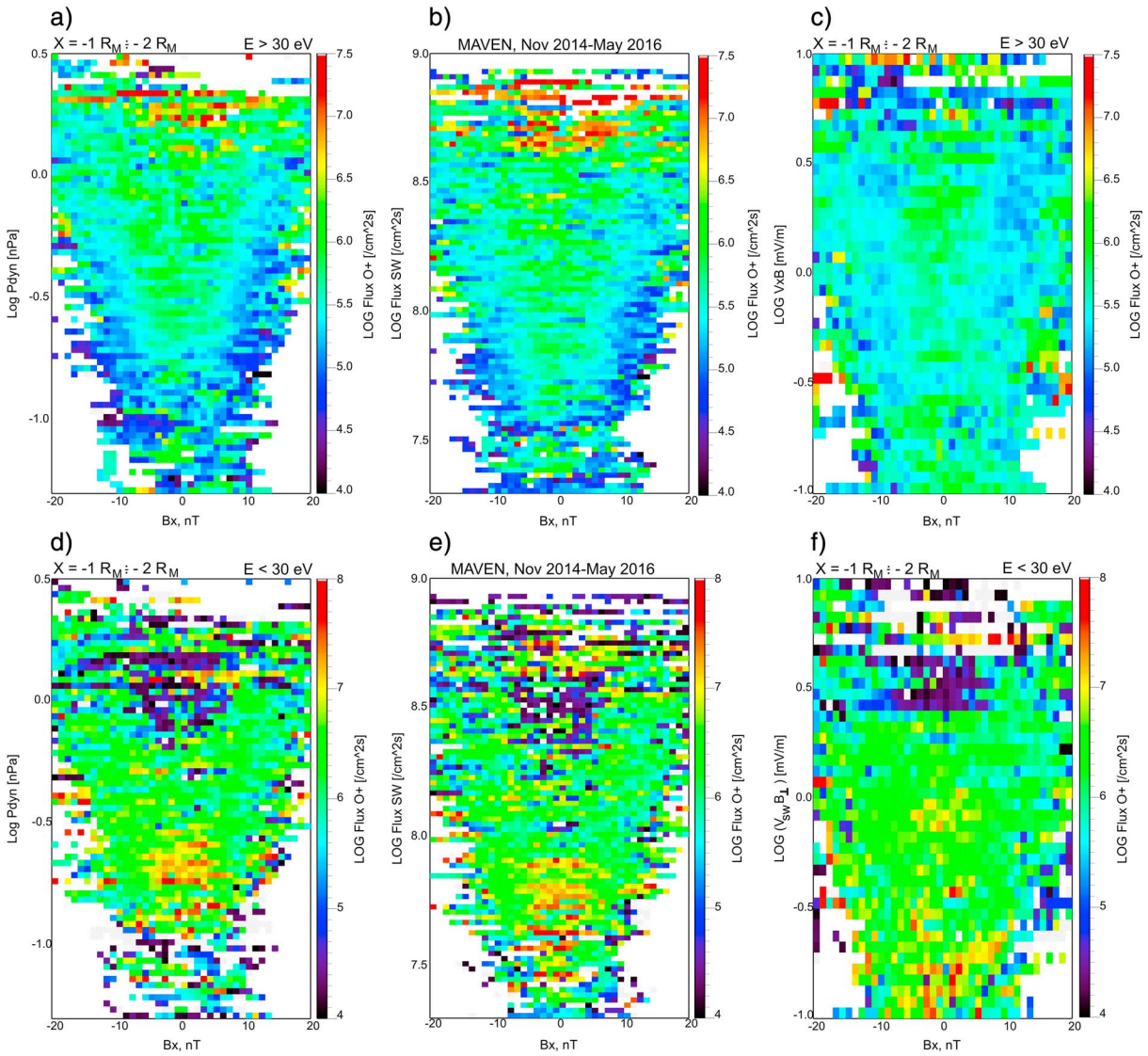

Figure 8. Maps of the mean values of fluxes of O+ ions with (a–c) $E > 30$ eV and (d–f) $E < 30$ eV across the tail as a function of the solar wind dynamic pressure (Figures 8a and 8d), the solar wind flux (Figures 8b and 8e), and the motional electric field in the solar wind (Figures 8c and 8f) at $-2\,R_M < X < -1\,R_M$.

is strongly asymmetrical (see Figure 3d). Higher fluxes are observed in the E^- hemisphere. To study the relationship between fluxes of oxygen ions and the conditions in the solar wind, we selected the parameter space 10 nT $< B_x <$ 20 nT at $-2\,R_M < X < -1\,R_M$ (see Figure 2b). Figure 10 shows how F_{O^+} depends on P_{dyn}, F_{sw}, E_{sw}, and the cone angle. Black (green) curves show the mean (median) values and their standard deviations of O^+ ion fluxes, respectively. These value characterize the averaged fluxes in the circular area. Blue (red) curves depict the mean (median) values of ion fluxes measured in the E^- hemisphere at $-0.5\,R_M < Y_{MSE} < 0.5\,R_M$ and $-1.4\,R_M < Z_{MSE} < 1.3\,R_M$. Fluxes in this region are approximately 7 times higher than the averaged values in the whole circular area. The observed dependences are similar to those in the plasma sheet indicating similar processes of ion drag by the magnetic field tensions in both regions.

3.4. Upstream and Magnetosheath

Ions extracted from the hot oxygen exosphere and the external layers of the ionosphere move like test particles gaining energy by acceleration in the $-V \times B$ electric field. These ions are accelerated to high energies filling mainly the region outside the induced Martian magnetosphere. Fluxes carried by pickup ions are lower than the fluxes of less energized planetary ions occupying the Martian magnetosphere. Figure 11 shows variations of the fluxes of O^+ ions with $E > 30$ eV and the values of their standard deviations observed outside of the nominal boundary of the Martian magnetosphere caused by the variations of the solar wind proton flux

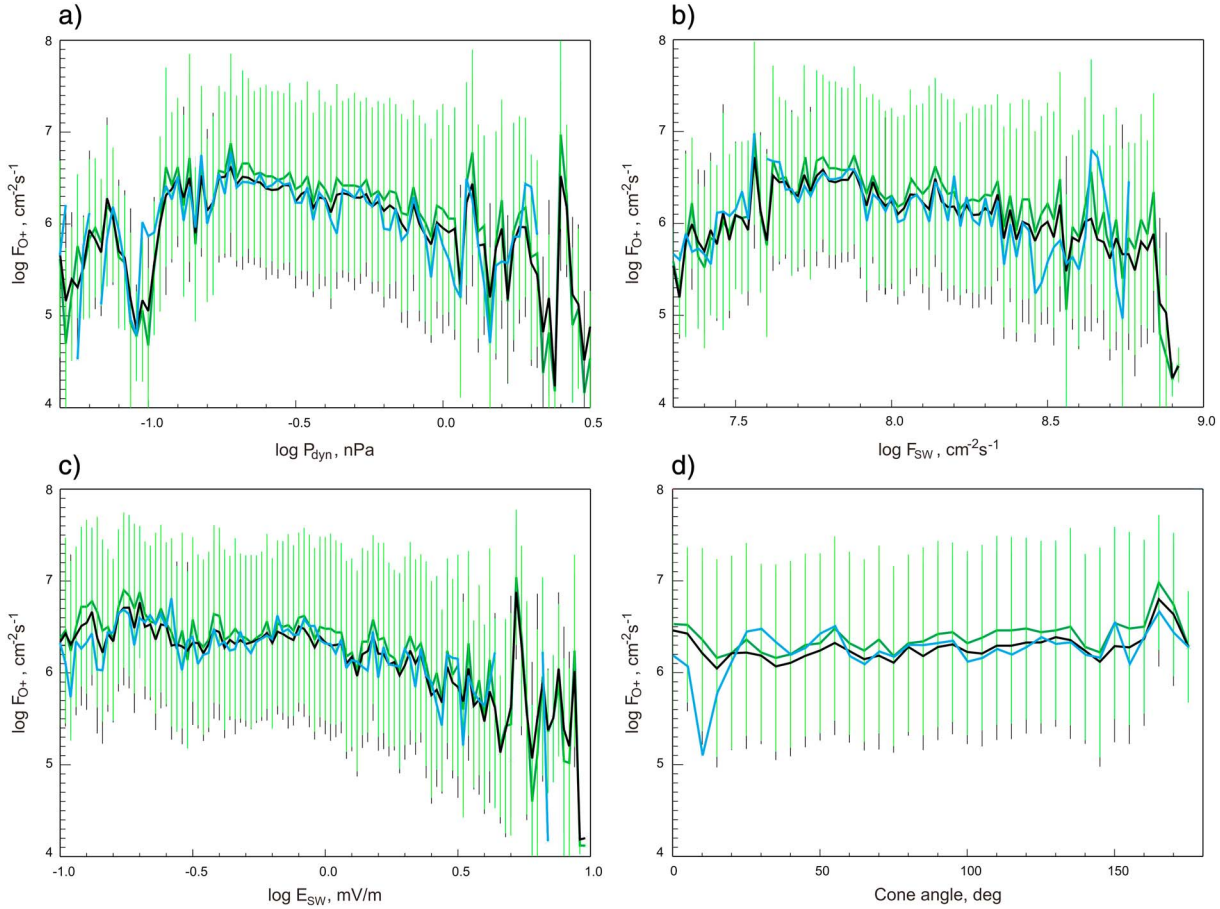

Figure 9. Mean (black) and median (green) values of fluxes of O^+ ions ($E < 30$ eV) and their standard deviations in the tail as a function of (a) the solar wind dynamic pressure, (b) the solar wind proton flux, (c) the motional electric field in the solar wind and (d) the IMF variations (the cone angle) at the distances $-2\,R_M < X < -1\,R_M$. Blue curves show the dependences of mean values of the ion fluxes at the fixed value (0.045–0.06 W/m^2) of the solar irradiance.

and the motional electric field. Black (blue) curves depict the measurements made in the E^- and E^+ hemispheres, respectively. At $F_{sw} \geq 6.3 \cdot 10^7$ cm^{-2} s^{-1} fluxes of the pickup O^+ ions rise with increasing solar wind flux. At $2 \cdot 10^7$ cm^{-2} $s^{-1} \leq F_{sw} \leq 6.3 \cdot 10^7$ cm^{-2} s^{-1} fluxes remain almost the same in the E^+ hemisphere, while in the E^- hemisphere, we observe the opposite trend—an enhancement of ion fluxes with decreasing solar wind flux. Note that a similar behavior for ions with $E > 30$ eV was also recorded in the E^- hemisphere but within the Martian magnetosphere (see Figure 6). Green curves show the ion fluxes measured outside of the nominal position of the Martian bow shock. Fluxes in this area are slightly lower but reveal similar variations with the solar wind flux. We also do not observe any noticeable variations with changes in the values of the motional electric field.

4. Discussion

Although the total ion losses at Mars and their dependence on the solar wind might be easily estimated by using cylindrical coordinates (see, e.g., Lundin et al., 2008; Nilsson et al., 2011; Ramstad et al., 2015), a lot of important features of the solar wind-Mars interaction are missed. As a result, the global picture of the Martian space environment occurs oversimplified. The utilization of MSE coordinates adds new pieces to this picture since the major part of the magnetosphere is formed by the IMF lines draping around the ionospherical obstacle. In this presentation, the important role of the motional electric field is revealed. The E^+-E^- hemispherical asymmetry in the magnetic field and the ion fluxes (including the appearance of the ion plume) is clearly displayed in the MSE coordinate system. However, even in such a description the global statistical picture occurs rather blurred because the IMF continuously varies forming a "nested" draping field configuration.

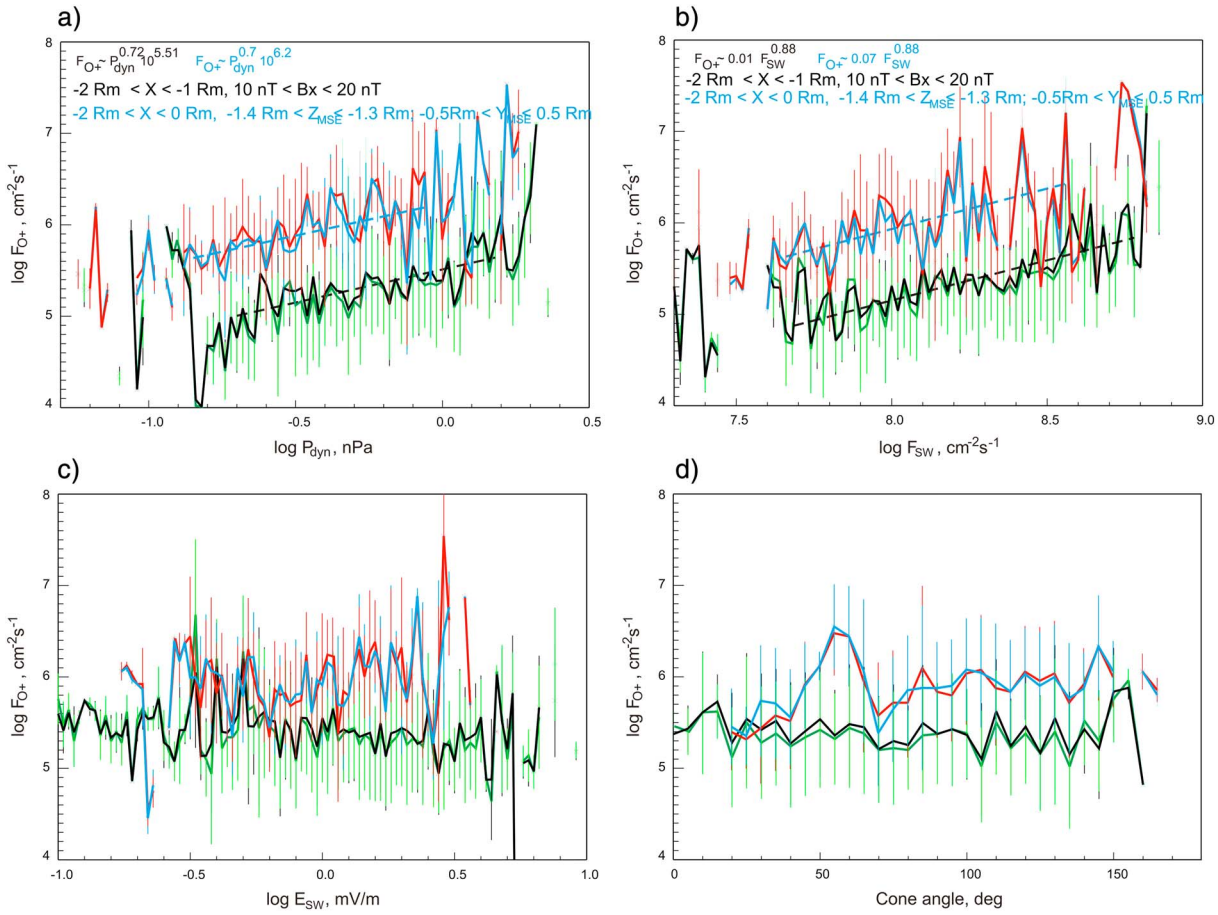

Figure 10. Black (green) curves show the averaged dependences of the mean (median) values of the ion fluxes and their standard deviations, respectively, on (a) P_{dyn}, (b) F_{sw}, (c) E_{sw}, and (d) the cone angle in the whole circular-shaped area behind Mars. Blue (red) curves depict such dependences in the E^- hemisphere where the fluxes are much higher.

Moreover, the existence of a time lag between the instantaneous IMF and the orientation of the tail lobes and the current sheet varying with the position in the magnetosphere additionally smears the picture. In this paper we used the modified MSE system in which, for example, instead of the Y_{MSE} axis the local B_x component in the tail was utilized. This allows to distinctly separate the tail lobes and the plasma sheet. It was shown

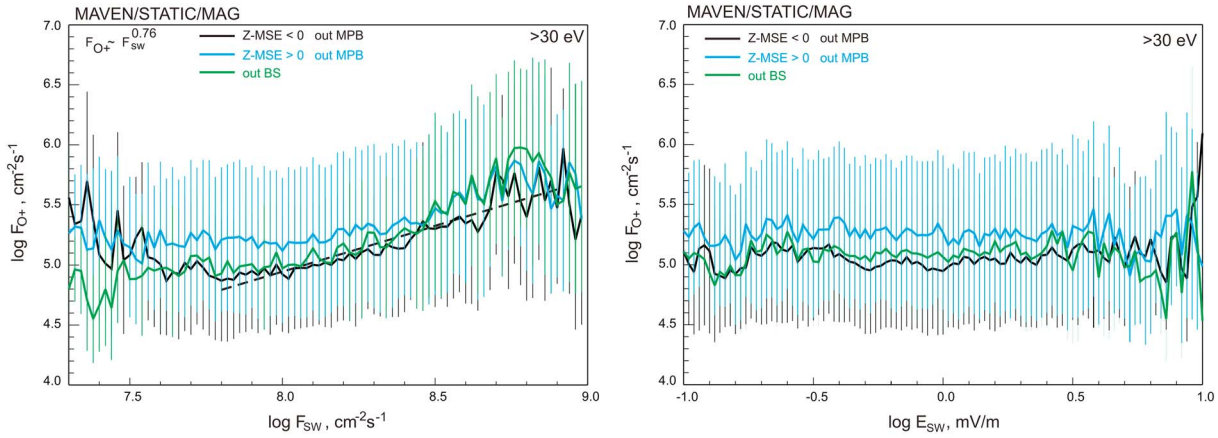

Figure 11. Mean values of fluxes of O^+ ions ($E > 30$ eV) and their standard deviations outside of the induced magnetosphere boundary as a function of (left) the solar wind proton flux and (right) the motional electric field in the solar wind. Black and blue curves show the fluxes in the E^- and E^+ hemisphere, respectively. The green curves depict the fluxes outside the Martian bow shock.

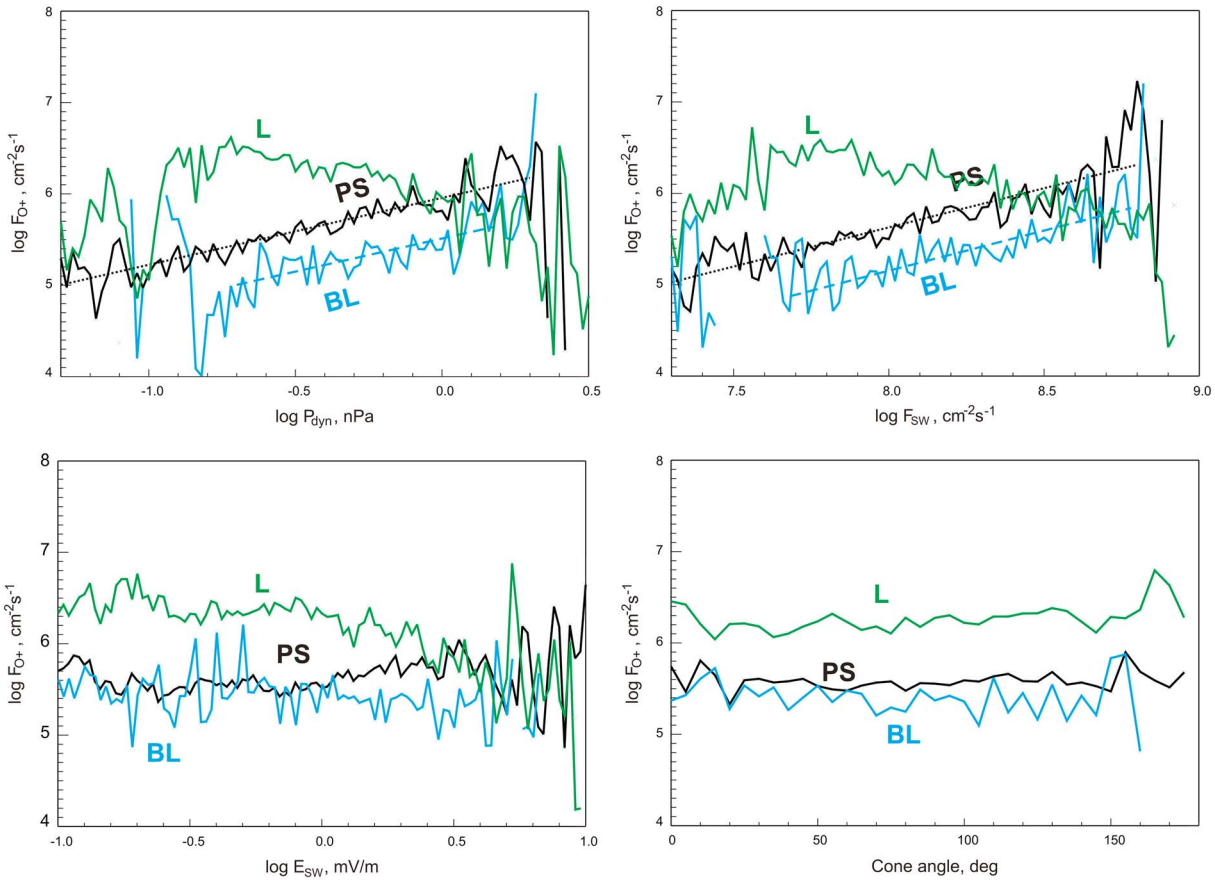

Figure 12. Mean values of fluxes of O^+ ions in the different escape channels (PS—plasma sheet, L—lobes, and BL—boundary layer) in the tail as functions of the conditions in the solar wind and the IMF.

that the tail lobes, where the B_x component dominates, are filled by the low-energy oxygen ions, while the plasma sheet contains the ions accelerated by the $j \times B$ force.

The filling of the tail is not symmetrical emphasizing the existence of two different main sources of supply of planetary plasma. The flux tubes passing through the E^- hemisphere, in which the magnetic field is less, have a larger cross-area A (the magnetic flux $B \times A$ is constant) as compared to the flux tubes moving in the E^+ ionosphere and therefore are more mass loaded by the photo-ions. We observe that the E^- ionosphere supplies the plasma sheet with a denser plasma and the filling occurs at larger distances (>2.5 R_M) in the tail.

The low-energy component, which mainly occupies the lobes, may be partly driven into tailward motion by the ambipolar electric field caused by the expansion of the ionospheric electrons along the field lines. Values of ion energy higher than expected for the common polar wind appear by ion preacceleration produced by a negative spacecraft potential as often observed in the Mars shadow. Mass-loaded pickup in which the ions are extracted from the dense ionosphere where the motional electric field is much less than in the solar wind and in the outer ionospheric regions and gain much less energy than in the classical pickup also contributes to the lobe population. The motional electric field imposes a strong asymmetry of fluxes of the low-energy ions through the E^+ and E^- hemispheres. The MAVEN observations show a shift of ion fluxes toward the E^- hemisphere. A similar asymmetry was observed in the near Venus tail (Dubinin et al., 2013).

Another region characterized by the enhanced fluxes of oxygen ions is the boundary layer which forms at the dayside. With transition to the nightside, the boundary layer shrinks taking the shape of a circular area with a strong asymmetry between E^+ and E^- hemispheres. In the E^- hemisphere ion fluxes are significantly higher. We assume that this ion population filling a circular area behind Mars is responsible for observations of the "tail rays" in the wake of Mars and Venus (Dubinin et al., 1991).

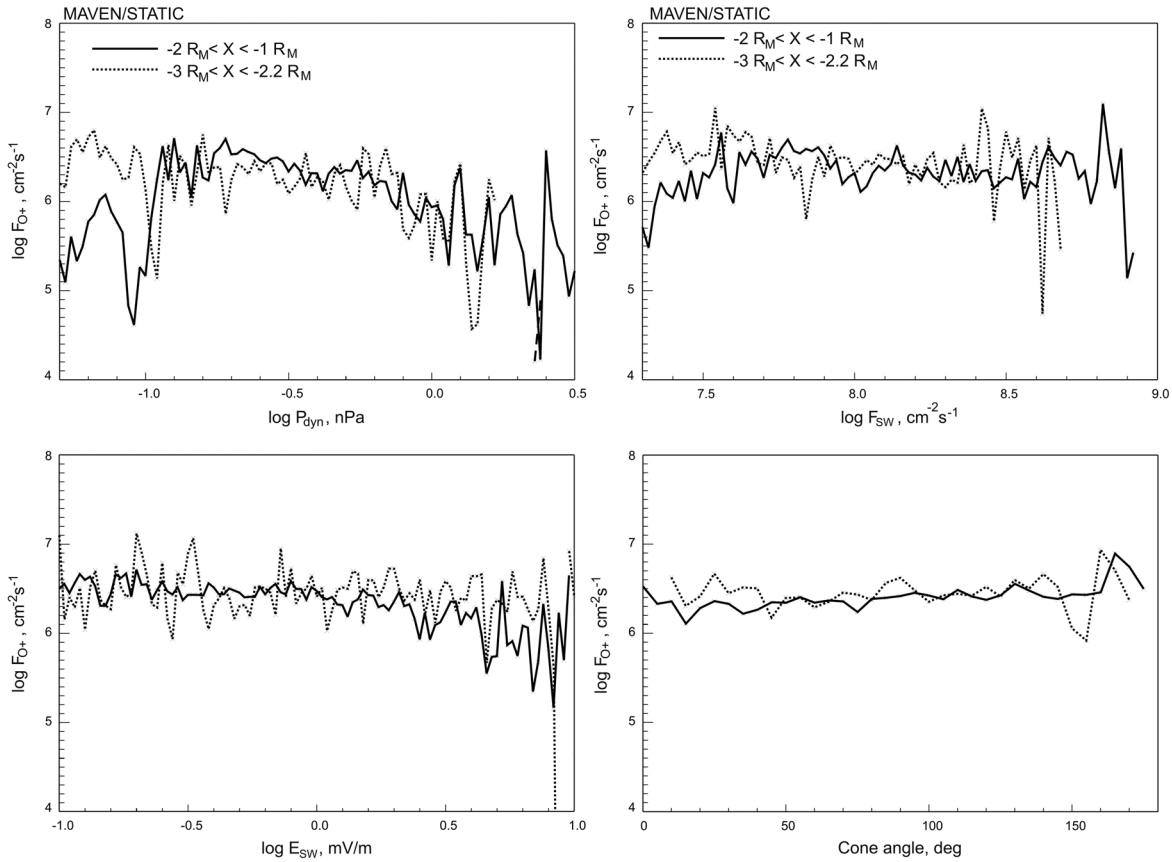

Figure 13. Mean values of the total values of the fluxes of O^+ ions as a functions of the conditions in the solar wind and the IMF.

Separating different escape routes, we have studied effects of the solar wind variability on the efficiency of ion losses through these channels. Figure 12 compares the dependences of ion fluxes in the tail on the solar wind and the IMF variations for the different escape channels. The almost linear dependence between ion flux in the near Mars plasma sheet and solar wind flux can be explained by the momentum transfer from the solar wind to the compressed magnetic field on the dayside (the magnetic pressure) and the following transfer of the momentum flux from the rising magnetic field tensions in the tail to the planetary ions (Dubinin & Fraenz, 2015; Dubinin et al., 2011). The absence of a relationship between the ion fluxes and the motional electric field implies the dominance of the $j \times B$ forces. Similar relations between O^+ ion fluxes in the boundary layer and the plasma sheet imply that the general mechanism of ion escape through these channels is governed by $j \times B$ forces.

On the other hand, values of fluxes of ions filling the plasma sheet from the E^- hemisphere also reveal a positive correlation with the motional electric field. This probably can be explained by the reduced values of the $j \times B$ forces in the E^- hemisphere in which the draped magnetic field is smaller, and therefore, by the enhanced role of the $V \times B$ term.

Another important feature is the observed enhancement of ion fluxes in the plasma sheet at $X \leq 2.2\,R_M$ at low values of the solar wind dynamic pressure and the solar wind flux. Although this unusual trend should be confirmed by larger statistics, we can speculate that at low values of the solar wind dynamic pressure, the ionosphere expands outward where it is more efficiently scavenged and transported to the plasma sheet. Since the expansion occurs not symmetrical with respect to the direction of the motional electric field, we observe such features in the plasma sheet which is filled from the E^- hemisphere.

A different trend is observed for the fluxes of O^+ ions with low energies ($E < 30$ eV). Except for very low values of the solar wind dynamic pressure and solar wind flux, we observe a decrease of the fluxes of the low-energy oxygen ions in the tail with an increase of the solar wind flux. It is important to note that the ion fluxes through the tail in the low-energy range dominate at $2 \cdot 10^7$ cm^{-2} s$^{-1} \leq F_{sw} \leq 3.16 \cdot 10^8$ cm^{-2} s^{-1}

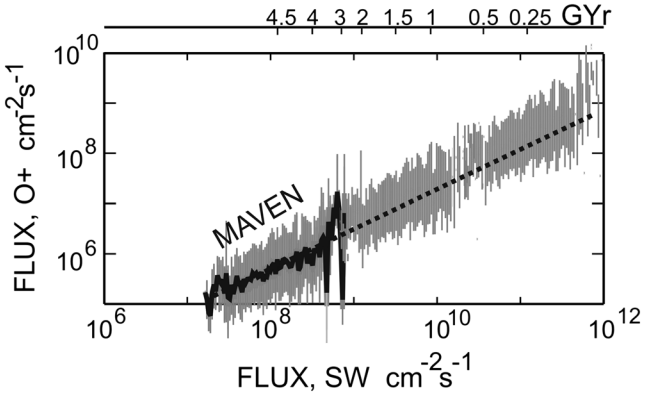

Figure 14. Extrapolation of the mean values of the fluxes of O^+ ions and its standard deviations as a functions of the solar wind flux to the past epoch.

and 0.2 nPa $\leq P_{dyn} \leq$ 1 nPa. A decrease of the fluxes of the low-energy ions with rising solar wind dynamic pressure and flux is probably related to the stronger energization of the ions driven by the $j \times B$ and $v \times B$ terms. Ions which gain an energy >30 eV appear in the other inventory. As a result, the net effect of variations of the total oxygen ion fluxes is rather small. Because of small variations of the total ion fluxes with the solar wind flux, we can easily estimate the total losses of oxygen ions through the tail at the given time interval. The averaged values of the escape rate of oxygen ions, including O_2^+ ions, are 6.2–7.35 $\times 10^{24}$ s^{-1}. Note that these values are probably somewhat underestimated for the reason of the possible positive spacecraft potential outside of the optical shadow.

A difference in the relationship between O^+ ion fluxes and solar wind variations for different escape channels and different ion energy ranges explains an inconsistency between previous studies. Lundin et al. (2008) analyzed the behavior of the heavy planetary ions with $E > 30$ eV for the period when ASPERA-3 was not measuring low-energy ions. The authors observed an increase of ion fluxes with increasing solar wind pressure. Such a positive correlation is in agreement with our observations for the energized ion component in the tail. On the other hand, analyzing the dynamics of the total ion losses through the tail including the low-energy ion component Nilsson et al. (2011) did not find noticeable variations in the total escape flows. According to our results, this can be explained by the major contribution of the low-energy ions whose fluxes decrease with increase of the solar wind dynamic pressure (flux). Similarly, the observations by Dubinin et al. (2011) and Dubinin and Fraenz (2015) of the almost linear dependence of the ion fluxes in the plasma sheet with the solar wind flux variations are well consistent with our finding for the plasma sheet. However, while considering the response of the total ion population in the tail, we can see even a decrease of ion fluxes at high values of the solar wind dynamic pressure (flux) (Figure 13) which is in agreement with the statistical studies by Ramstad et al. (2015) based on the MEX/ASPERA-3 observations.

The important question remains about ion losses at Mars in the early epochs when the solar wind was much stronger (Lundin et al., 2007) . Inspecting again Figure 12, we can assume that with the further increase of the solar wind dynamic pressure (flux), the contribution of the energized ($E > 30$ eV) ion component will more and more dominate in the total fluxes and these fluxes will gradually occupy the whole tail. As a result, we can extrapolate the behavior of the ion fluxes in the plasma sheet and the boundary layer to earlier epochs (Figure 14). According to this extrapolation, the mean values of the escape fluxes of O^+ ions could reach $\sim 10^9$ cm^{-2} s^{-1}. It is worth noting that this estimate is very conservative since the solar irradiance in the past epoch was much higher than now and ion fluxes of the low-energy ion component significantly increase with increase of the solar EUV fluxes (Dubinin, Fraenz, Pätzold, Andrews, et al., 2017; Dubinin, Fraenz, Pätzold, McFadden, et al., 2017). The enhancement of the ionospheric pressure with the EUV flux can change the state of the ionosphere from a "magnetized" to an "unmagnetized" that can drastically change the escape processes.

In conclusion, we note that in future studies one should improve the used modified MSE system by sorting the different types of field lines distinguishing the open and closed field lines. The rotation of the spacecraft orbits into the MSE frame, and the averaging of ion fluxes significantly reduces the identification of a possible role of the crustal magnetic fields. As a result, a global effect of the crustal fields remains hidden. The utilization of MSO coordinates with a fixed sign of the B_y-IMF component reveals new elements of the Martian magnetosphere. Due to the contribution of the low-order harmonics of the crustal magnetic field and the draping IMF, the magnetosphere acquires the properties of a combined magnetosphere (Dubinin et al., 1980). The existence of different classes of the magnetic field lines in the near Mars tail might be responsible for the observed large standard deviations from the averaged values of the ion fluxes at Mars. Indeed, a large variety of the current sheet features with different pressure balances observed by Artemyev et al. (2017) indicates the existence of different regimes of the magnetic field tension release and plasma transport in the Martian tail.

Acknowledgments
The MAVEN project is supported by NASA through the Mars Exploration Program. MAVEN data are publicly available through the Planetary Data System. Authors E. D. and M. P. wish to acknowledge support from DFG for supporting this work by grant PA 525/14-1. Authors E. D. and M. F. wish to acknowledge support from DLR by grant 50QM1703. O. V. and L. Z. wish to acknowledge support from the Russian Science Foundation by grant 16-42-01 103.

References

Acuña, M., Connerney, J. E. P, Wasilewski, P., Lin, R. P., Anderson, K. A., Carlson, C. W., … Ness, N. F. (1998). Magnetic field and plasma observations at Mars: Initial results of the Mars Global Surveyor mission. *Science*, *279*(5357), 1676–1680. https://doi.org/10.1126/science.279.5357.1676

Artemyev, A., Angelopoulos, V., Halekas, J. S., Runov, A., Zelenyi, L. M., & McFadden, J. P. (2017). Mars magnetotail: Nature's current sheet laboratory. *Journal of Geophysical Research: Space Physics*, *122*, 5404–5417. https://doi.org/10.1002/2017JA024078

Barabash, S., Dubinin, E., Pissarenko, N., Lundin, R., & Russell, C. T. (1991). Picked-up protons near Mars: Phobos observations. *Geophysical Research Letters*, *18*(10), 1805–1808. https://doi.org/10.1029/91GL02082

Barabash, S., Fedorov, A., Lundin, R., & Sauvaud, J. A. (2007). Martian atmospheric erosion rates. *Science*, *315*, 501–503. https://doi.org/10.1126/science.1134358

Brain, D., Bagenal, F., Acñna, M., & Connerney, J. (2003). Martian magnetic morphology: Contributions from the solar wind and crust. *Journal of Geophysical Research*, *108*(A12), 1424. https://doi.org/10.1029/2002JA009482

Brain, D., Lillis, R., Mitchell, D., Halekas, J., & Lin, R. (2007). Electron pitch angle distributions as indicators of magnetic field topology near Mars. *Journal of Geophysical Research*, *112*, A09201. https://doi.org/10.1029/2007JA012435

Cain, J. C., Ferguson, B. B., & Mozzoni, D. (2003). An n = 90 internal potential function of the Martian crustal magnetic field. *Journal of Geophysical Research*, *108*, 5008. https://doi.org/10.1029/2000JE001487

Collinson, G., Mitchell, D., Glocer, A., Grebowsky, J., Peterson, W. K., Connerney, J., … Jakosky, B. (2015). Electric Mars: The first direct measurement of an upper limit for the Martian "polar wind" electric potential. *Geophysical Research Letters*, *42*, 9128–9134. https://doi.org/10.1002/2015GL065084

Connerney, J. E. P., Espley, J., Lawton, P., Murphy, S., Odom, J., Oliversen, R., & Sheppard, D. (2015). The MAVEN magnetic field investigation. *Space Science Reviews*, *195*(1-4), 257–291. https://doi.org/10.1007/s11214-015-0169-4

DiBraccio, G. A., Dann, J., Espley, J. R., Gruesbeck, J. R., Soobiah, Y., Connerney, J. E. P., … B. M. Jakosky (2017). MAVEN observations of tail current sheet flapping at Mars. *Journal of Geophysical Research: Space Physics*, *122*, 4308–4324. https://doi.org/10.1002/2016JA023488

Dong, Y., Fang, X., Brain, D. A., McFadden, J. P., Halekas, J. S., Connerney, J. E., … Jakosky, B. M. (2015). Strong plume fluxes at Mars observed by MAVEN: An important planetary ion escape channel. *Geophysical Research Letters*, *42*, 8942–8950. https://doi.org/10.1002/2015GL065346

Dong, Y., Fang, X., Brain, D. A., McFadden, J. P., Halekas, J. S., Connerney, J. E. P., … Jakosky, B. M. (2017). Seasonal variability of Martian ion escape through the plume and tail from MAVEN observations. *Journal of Geophysical Research: Space Physics*, *122*, 4009–4022. https://doi.org/10.1002/2016JA023517

Dubinin, E., & Fraenz, M. (2015). Magnetotails of Mars and Venus. *Geophysical Monograph Series*, *207*, 43–59. https://doi.org/10.1002/9781118842324.ch3

Dubinin, E., Fraenz, M., Fedorov, A., Lundin, R., Edberg, N., Duru, F., & Vaisberg, O. (2011). Ion energization and escape on Mars and Venus. *Space Science Reviews*, *162*, 173–211. https://doi.org/10.1007/978-1-4614-3290-6-6

Dubinin, E., Fraenz, M., Pätzold, M., Andrews, D., Vaisberg, O., Zelenyi, L., & Barabash, S. (2017). Martian ionosphere observed by Mars Express: 2. Influence of solar irradiance on upper ionosphere and escape fluxes. *Planetary and Space Science*, *144*, 1–8.

Dubinin, E., Fraenz, M., Pätzold, M., McFadden, J., Mahaffy, P. R., Eparvier, F., … Zelenyi, L. (2017). Effects of solar irradiance on the upper ionosphere and oxygen ion escape at Mars: MAVEN observations. *Journal of Geophysical Research: Space Physics*, *122*, 7142–7152. https://doi.org/10.1002/2017JA024126

Dubinin, E., Fraenz, M., Woch, J., Barabash, S., Lundin, R., & Yamauchi, M. (2006). Hydrogen exosphere at Mars: Pickup protons and their acceleration at the bow shock. *Geophysical Research Letters*, *33*, L22103. https://doi.org/10.1029/2006GL027799

Dubinin, E., Fraenz, M., Woch, J., Zhang, T. L., Wei, Y., Fedorov, A., … Lundin, R. (2012). Bursty escape fluxes in plasma sheets of Mars and Venus. *Geophysical Research Letters*, *39*, L01104. https://doi.org/10.1029/2011GL049883

Dubinin, E., Fraenz, M., Zhang, T. L., Woch, J., Wei, Y., Fedorov, A., … Lundin, R. (2013). Plasma in the near Venus tail: Venus Express observations. *Journal of Geophysical Research: Space Physics*, *118*, 7624–7634. https://doi.org/10.1002/2013JA019164

Dubinin, E., Franz, M., Woch, J., Roussos, E., Barabash, S., Lundin, R., … Acuña, M. (2006). Plasma morphology at Mars: ASPERA-3 observations. *Space Science Reviews*, *126*, 209–238. https://doi.org/10.1007/s11214-006-9039-4

Dubinin, E., Israelevich, P. L., & Podgomy, I. M. (1980). Combined magnetosphere. *Cosmic Research, Engl. Trans1.*, *18*(470), 1980.

Dubinin, E., Lundin, R., Norberg, O., & Pissarenko, N. (1993). Ion acceleration in the Martian tail: Phobos observations. *Journal of Geophysical Research*, *98*, 3991–3997. https://doi.org/10.1029/92JA02233

Dubinin, E., Lundin, R., Riedler, W., Schwingenschuh, K., Luhmann, J. G., Russell, C. T., & Brace, L. H. (1991). Comparison of observed plasma and magnetic field structures in the wakes of Mars and Venus. *Journal of Geophysical Research*, *96*(A7), 11,189–11,197.

Dubinin, E., Lundin, R., & Schwingenschuh, K. (1994). Solar wind electrons as tracers of the Martian magnetotail topology. *Journal of Geophysical Research*, *99*, 21,233–21,240.

Dubinin, E., Sauer, K., Lundin, R., Norberg, O., Trotignon, J-G., Schwingenschuh, K., … Riedler, W. (1996). Plasma characteristics of the boundary layer in the Martian magnetosphere. *Journal of Geophysical Research*, *101*(A12), 27,061–27,075.

Eparvier, F. G., Chamberlin, P. C., Woods, T. N., & Thiemann, E. M. B. (2015). The solar extreme ultraviolet monitor for MAVEN. *Space Science Reviews*, *195*, 293–301. https://doi.org/10.1007/s11214-015-0195-2

Fang, X., Ma, Y., Brain, D., Dong, Y., & Lillis, R. (2015). Control of Mars global atmospheric loss by the continuous rotation of the crustal magnetic field: A time-dependent MHD study. *Journal of Geophysical Research: Space Physics*, *120*, 10,926–10,944. https://doi.org/10.1002/2015JA021605

Fedorov, A., Budnik, E., Sauvaud, J.-A., Mazelle, C., Barabash, S., Lundin, R., … Dierker, C. (2006). Structure of the Martian wake. *Icarus*, *182*, 329–336. https://doi.org/10.1016/j.icarus.2005.09.021

Fedorov, A., Ferrier, C., Sauvaud, J. A., Barabash, S., Zhang, T. L., Mazelle, C., … Bochsler, P. (2008). Comparative analysis of Venus and Mars magnetotails. *Planetary and Space Science*, *56*, 812–817. https://doi.org/10.1016/j.pss.2007.12.012

Fräenz, M., Dubinin, E., Andrews, D., Nilsson, H., Barabash, S., & Fedorov, A. (2015). Cold ion escape from the Martian ionosphere. *Planetary and Space Science*, *119*, 92–102. https://doi.org/10.1016/j.pss.2015.07.012

Jakosky, B. M., Lin, R. P., Grebowsky, J. M., Luhmann, J. G., Mitchell, D. F., Beutelschies, G., … Zurek, R. (2015). The Mars Atmosphere and Volatile EvolutioN (MAVEN) mission. *Space Science Reviews*, *195*(1-4), 3–48. https://doi.org/10.1007/s11214-015-0139-x

Halekas, J., Taylor, E., Dalton, G., Johnson, G., Curtis, D., McFadden, J., … Jakosky, B. (2015). The solar wind ion analyzer for MAVEN. *Space Science Reviews*, *195*, 125–151. https://doi.org/10.1007/s11214-013-0029-z

Halekas, J. S., Brain, D. A., Lillis, R. J., Fillingim, M. O., Mitchell, D. L., & Lin, R. P. (2006). Current sheets at low altitudes in the Martian magnetotail. *Geophysical Research Letters*, *33*, L13101. https://doi.org/10.1029/2006GL026229

Halekas, J. S., Ruhunusiri, S., Harada, Y., Collinson, G., Mitchell, D. L., Mazelle, C., … Jakosky, B. M. (2017). Structure, dynamics, and seasonal variability of the Mars-solar wind interaction: MAVEN solar wind ion analyzer inflight performance and science results. *Journal of Geophysical Research: Space Physics*, *121*, 547–578. https://doi.org/10.1002/2016JA023167

Luhmann, J. G., Dong, C. F., Ma, Y. J., Curry, S. M., Xu, S., Lee, C. O., … Jakosky, B. M. (2017). Martian magnetic storms. *Journal of Geophysical Research: Space Physics*, *122*, 6185–6209. https://doi.org/10.1002/2016JA023513

Lundin, R., Barabash, S., Fedorov, A., Holmström, M., Nilsson, H., Sauvaud, J.-A., & Yamauchi, M. (2008). Solar forcing and planetary ion escape from Mars. *Geophysical Research Letters*, *35*, L09203. https://doi.org/10.1029/2007GL032884

Lundin, R., Lammer, H., & Ribas, I. (2007). Planetary magnetic fields and solar forcing: Implications for atmospheric evolution. *Space Science Reviews*, *129*, 245–278. https://doi.org/10.1007/s11214-007-9176-4

Ma, Y., Fang, X., Russell, C. T., Nagy, A. F., Toth, G., & Luhmann, J. G. (2014). Effects of crustal field rotation on the solar wind plasma interaction with Mars. *Geophysical Research Letters*, *41*, 6563–6569. https://doi.org/10.1002/2014GL060785

McFadden, J. P., Kortmann, O., Curtis, D., Dalton, G., Johnson, G., Abiad, R., … Jakosky, B. (2015). MAVEN SupraThermal and Thermal Ion Compostion (STATIC) instrument. *Space Science Reviews*, *195*, 199–256. https://doi.org/10.1007/s11214-015-0175-6

Modolo, R., Chanteur, G. M., & Dubinin, E. (2012). Dynamic Martian magnetosphere: Transient twist induced by a rotation of the IMF. *Geophysical Research Letters*, *39*, L01106. https://doi.org/10.1029/2011GL049895

Nagy, A. F., Winterhalter, D., Sauer, K., Cravens, T. E., Brecht, S., Mazelle, C., … Trotignon, J. G. (2004). The plasma environment of Mars. *Space Science Reviews*, *111*, 33. https://doi.org/10.1023/B: SPAC.0000032718.47512.92

Nilsson, H., Carlsson, E., Brain, D. A., Yamauchi, M., Holmström, M., Barabash, S., … Futaana, Y. (2010). Ion escape from Mars as a function of solar wind conditions: A statistical study. *Icarus*, *206*(1), 40–49. https://doi.org/10.1016/j.icarus.2009.03.006

Nilsson, H., Edberg, N. J. T., Stenberg, G., Barabash, S., Holmstrom, M., Futaana, Y., … Fedorov, A. (2011). Heavy ion escape from Mars, influence from solar wind conditions and crustal magnetic fields. *Icarus*, *215*, 475–484. https://doi.org/10.1016/j.icarus.2011.08.003

Nilsson, H., Stenberg, G., Futaana, Y., Holmstrom, M., Barabash, S., Lundin, R., … Fedorov, A. (2012). Ion distributions in the vicinity of Mars: Signatures of heating and acceleration processes. *Earth Planets Space*, *64*, 135–148.

Nordstrom, T., Stenberg, G., Nilsson, H., Barabash, S., & Zhang, T. L. (2013). Venus ion outflow estimates at solar minimum: Influence of reference frames and disturbed solar wind conditions. *Journal of Geophysical Research: Space Physics*, *118*, 3592–3601. https://doi.org/10.1002/jgra.50305

Rahmati, A., Larson, D. E., Cravens, T. E., Lillis, R. J., Dunn, P. A., Halekas, J. S., … Jakosky, B. M. (2015). MAVEN insights into oxygen pickup ions at Mars. *Geophysical Research Letters*, *42*, 8870–8876. https://doi.org/10.1002/2015GL065262

Rahmati, A., Larson, D. E., Cravens, T. E., Lillis, R. J., Halekas, J. S., McFadden, J. P., … Jakosky, B. M. (2017). MAVEN measured oxygen and hydrogen pickup ions: Probing the Martian exosphere and neutral escape. *Journal of Geophysical Research: Space Physics*, *122*, 3689–3706. https://doi.org/10.1002/2016JA023371

Ramstad, R., Barabash, S., Futaana, Y., Nilsson, H., Wang, X.-D., & Holmstrom, M. (2015). The Martian atmospheric ion escape rate dependence on solar wind and solar EUV conditions: 1. Seven years of Mars Express observations. *Journal of Geophysical Research: Planets*, *120*, 1298–1309. https://doi.org/10.1002/2015JE004816

Vaisberg, O. (1976). Mars-plasma environment, *Physics of solar planetary environment* (pp. 854–873).

Xu, S., Mitchell, D., Liemohn, M., Dong, C., Bougher, S., Fillingim, M., … Jakosky, B. (2016). Deep nightside photoelectron observations by MAVEN SWEA: Implications for Martian northern hemispheric magnetic topology and nightside ionosphere source. *Geophysical Research Letters*, *43*, 8876–8884. https://doi.org/10.1002/2016GL070527

Xu, S., Mitchell, D., Liemohn, M., Dong, C., Bougher, S., Fillingim, M., … Jakosky, B. (2017). Martian low-altitude magnetic topology deduced from MAVEN/SWEA observations. *Journal of Geophysical Research: Space Physics*, *122*, 1831–1852. https://doi.org/10.1002/2016JA023467

Yamauchi, M., Futaana, Y., Fedorov, A., Dubinin, E., Lundin, R., Sauvaud, J.-A., … Luhmann, J. (2006). IMF direction derived from cycloid-like ion distributions observed by Mars Express. *Space Science Reviews*, *126*, 239–266.

Yamauchi, M., Hara, T., Lundin, R., Dubinin, E., Fedorov, A., Sauvaud, J.-A., … Barabash, S. (2015). Seasonal variation of Martian pick-up ions: Evidence of breathing exosphere. *Planetary and Space Science*, *119*, 54–61. https://doi.org/10.1016/j.pss.2015.09.013

Yeroshenko, Y., Riedler, W., Schwingenschuh, K., Luhmann, J. G., Ong, M., & Russell, C. T. (1990). The magnetotail of Mars: Phobos observation. *Geophysical Research Letters*, *17*, 885–888. https://doi.org/10.1029/GL017i006p00885